

# Simulations of Protostar-Driven Photoionization in Herbig-Haro Jets

Z. Ahmane<sup>1,2</sup>, A. Mignone<sup>2</sup>, C. Zanni<sup>2</sup>, S. Massaglia<sup>2</sup>, and A. Bouldjderi<sup>1</sup>

<sup>1</sup>Hadj Lakhdar Batna 1 University, Algeria

<sup>2</sup>Università degli Studi di Torino, Italy  
zoubida.ahmane@edu.unito.it

## Abstract

Recent studies showed that observations of line emission from shocks in YSO jets require a substantial amount of ionization of the pre-shock matter. Photoionization from X-ray emitted close to the central source may be responsible for the initial ionization fraction. The aim of our work is to study the effect of X-ray photoionization, coming from the vicinity of the central star, on the ionization fraction inside the jet that can be advected at large distances. For this purpose we have performed axisymmetric MHD jet launching simulations including photoionization and optically thin losses using PLUTO. For typical X-ray luminosities in classical T-Tauri stars, we see that the photoionization is responsible for ionizing to 10 % -20 % the jet close to the star.

**keywords** YSO- jets , X-rays, Hydrodynamics, Methods: Numerical, Magnetohydrodynamics: MHD, Astrophysics

## 1 Introduction

A protostellar jet is a highly supersonic, magnetised and collimated outflow which heralds the birth of star while it is still embedded, out of sight, in its molecular cocoon. In particular, Herbig Haro (HH) jets like HH30, DG tau, RW Aur [Bacciotti and Eisloffel, 1999, Lavalley et al., 1997, Lavalley-Fouquet et al., 2000, Bacciotti et al., 2002, Melnikov et al., 2009] are detected in star forming regions T-Tauri stars and are characterised by highly collimated ejection of matter, emanating directly from the regions surrounding the protostars [Reipurth et al., 1986, Mundt, 1986, Lada, 1985, Maurri et al., 2014], and associated with line emissions being identified as due to shocked gas that has been heated and compressed [Schwartz, 1975, Dopita, 1978] by various nonlinear Magneto-Hydrodynamic (MHD)

effects, such as shear-layer instabilities [Massaglia et al., 1992, Hardee et al., 1997, Micono et al., 2000], and/or by time variability in the accretion/ejection processes that steepen into shocks [Raga and Cantó, 1995, De Colle et al., 2008]. The modeling - either theoretical or numerical - of these magnetised supersonic shocked outflows, in presence of non equilibrium cooling and heating due to different physical processes, can lead to the interpretation of the physical aspects of the jet phenomenology and to set constraints on the main jet parameters. This is the reason an extensive effort is being put by several authors into modelling jet dynamics alongside radiation effects [Rossi et al., 1997, Shang et al., 2002, Moraghan et al., 2006, Teşileanu et al., 2008, Teşileanu et al., 2012, Teşileanu et al., 2014, Rubini et al., 2014, Gardner et al., 2017].

The basic aspects of the protostellar outflows are known since many decades. The outflow phase lasts for a long dynamical scale at least  $10^5$  yr e.g. Class I stars. They are  $\geq 10^3 - 10^4$  AU long [Bally et al., 2007] and have velocities of order of  $v_{\text{jet}} = 100 - 800 \text{ km s}^{-1}$ , increasing with central mass star [Eisloffel and Mundt, 1992, Eisloffel et al., 1994]. HH jets are very well collimated [Ray et al., 1996], with the jet radii  $\sim 50$  AU [Dougados et al., 2000], and are powered by accretion onto the central protostar [Cabrit et al., 1990, Hartigan et al., 1995, Livio, 1999]. The jet acceleration mechanisms proposed in the literature are: i) the magneto-centrifugal launch of the so-called "Disk-Winds" [Blandford and Payne, 1982], ii) thermal pressure at the base of the jets that produces "stellar winds" [Sauty and Tsinganos, 1994, Sauty et al., 2002], and iii) the interaction processes that connect the stellar magneto-spheres with the disk to produce "X-winds" [Shu et al., 1994, Cai et al., 2008]. Disk and stellar wind acceleration mechanisms can well be both at work, as discussed by [Matsakos et al., 2008, Matsakos et al., 2009].

Numerical simulations of HH jets must deal with spatial scales that range from few AU up to tens of thousands of AUs, since the emission is actually observed on all scales and comes from post-shock regions. Over these regions line emission is observed at all scales, providing information about the physical parameters and - indirectly - about the morphologies. Even with the adoption of the most advanced Adaptive-Mesh-Refinement (AMR) techniques is nowadays impossible to perform a global, fully 3D MHD, simulation that includes the jet launching treatment up to the jet termination and, at the same time, maintains a sufficient spatial resolution for resolving shocks that arise along the jet.

Thus, large scale simulations typically begin at about 100 AUs from the jet origin and the jet itself is injected into the numerical domain setting reasonable, by somewhat arbitrary, initial and boundary conditions. Then the models follow the propagation of the jet and its interaction with the ambient medium [Moraghan et al., 2006, Favata et al., 2002, Stone et al., 1997, Teşileanu et al., 2012, Teşileanu et al., 2014]. These simulations can include the treatment of radiative cooling and heating and can produce synthetic maps of brightness, in the various lines, and allow for detailed comparison with observations.

A complementary approach adopted in the literature is to simulate, consistently, the jet launching and its propagation up to about 100 AUs. This is done either by considering the accretion disk and the jet evolution in the computa-

tion [Uchida and Shibata, 1985, Casse and Keppens, 2002, Meliani et al., 2006, Zanni et al., 2007, Tzeferacos et al., 2009, Teşileanu et al., 2012], or by assuming the disk as an imposed boundary condition [Ouyed and Pudritz, 1997, Fendt, 2009, Fendt, 2006, Matsakos et al., 2012]. Axisymmetrical numerical simulations of protostellar magnetised jets, that include launching and large scale simultaneously, have been performed [Ramsey and Clarke, 2011], but in the limits of ideal MHD.

The observed line emission is produced by the shocked gas in the regions lying behind the shock front. Radiative shocks have been studied in 1D steady state by [Cox and Raymond, 1985, Hartigan et al., 1994], they derived the post shock behaviour of various physical parameters (temperature, ionization fraction, electron density, etc). The 1D time dependent have been carried by [Massaglia et al., 2005, Teşileanu et al., 2009] they study the evolution of magnetised radiating shocks. 2D numerical study of radiating magnetised shocks along axisymmetric jet simulation have been performed by [Teşileanu et al., 2012] they were produced by imposing a sinusoidal perturbation on the jet base.

[Teşileanu et al., 2012] have found that an ionization fraction of  $\sim 10 - 20\%$  is necessary to obtain a closer agreement between observed brightness distributions in the different emission lines and simulated ones. They argued that the ionization may be provided by high energy photons coming from the embedded hot luminous protostars, that are X-rays emitting sources with luminosities  $L_x = 10^{28} - 10^{32} \text{ erg s}^{-1}$  [Favata et al., 2002, Bally et al., 2003, Skinner et al., 2011], and that this ionization persists for long distances along the jet because of the long recombination timescales.

Our goal in this paper is to verify the validity this basic hypothesis by considering the launching and large scale regions, simultaneously, and treating, along with the MHD processes, the heating and photoionization by X-rays, and the radiative cooling. As discussed before, this is somewhat challenging because of the large dynamical range involved. The simulations are carried out in 2D and employ AMR techniques.

The plan of the paper is the following: in Sect. 2 we discuss the model that includes cooling and photoionization due to X-rays, in Sect. 3 we outline the initial conditions and the computational scheme adopted; in Sect. 4 we examine the effect of X-rays on the ionization of the jet and the shock evolution, while in Sect. 5 we discuss the results and make comparisons with observations. Conclusions are drawn in Sect. 6.

## 2 Model

Our model consists of a time-dependent jet accelerated by underlying accretion disk set as a boundary conditions. The equations of magnetohydrodynamics are solved using the PLUTO code [Mignone et al., 2007, Mignone et al., 2012] by taking into account non-ideal effects due to radiative losses.

## 2.1 Governing Equations

In what follows, the fluid density, velocity, magnetic field and thermal pressure will be denoted, respectively, with  $\rho$ ,  $\mathbf{v}$ ,  $\mathbf{B}$  and  $P$ . The gas pressure depends on the plasma density  $\rho$ , temperature  $T$  and composition through the relation  $P = \rho k_B T / (\mu m_H)$ , where  $\mu$  is the mean molecular weight and  $k_B$  is the Boltzmann constant.

The code numerically solves the equation for the mass conservation:

$$\frac{\partial \rho}{\partial t} + \nabla \cdot (\rho \mathbf{v}) = 0, \quad (1)$$

momentum conservation:

$$\frac{\partial \rho \mathbf{v}}{\partial t} + \nabla \cdot \left[ \rho \mathbf{v} \mathbf{v} + P_t - \mathbf{B} \mathbf{B} \right] = -\rho \nabla \Phi_G = 0, \quad (2)$$

magnetic induction (Faraday's law):

$$\frac{\partial \mathbf{B}}{\partial t} - \nabla \times (\mathbf{v} \times \mathbf{B}) = 0, \quad (3)$$

and total energy conservation:

$$\frac{\partial e}{\partial t} + \nabla \cdot \left[ (e + P_t) \mathbf{v} - \mathbf{B}(\mathbf{v} \cdot \mathbf{B}) \right] = -\Lambda_c + \mathcal{H}_x. \quad (4)$$

In the expressions above,  $P_t = p + \mathbf{B}^2/2$  is the total (gas + magnetic) pressure,  $\Phi_G$  is the gravitational potential described (see below) while

$$e = \frac{P}{\gamma - 1} + \frac{\rho \mathbf{v}^2}{2} + \frac{\mathbf{B}^2}{2} + \rho \Phi_G, \quad (5)$$

is the total energy density with  $\Gamma = 5/3$  being the specific heat ratio. Note that a factor  $\sqrt{4\pi}$  has been conveniently re-absorbed in the definition of  $\mathbf{B}$ .

We adopt the SNEq (Simplified Non-Equilibrium cooling, see [Rossi et al., 1997, Teşileanu et al., 2008]) treatment of the radiative losses. This cooling function includes line emission from nine elements: H and He resonance lines, and the 13 strongest forbidden lines of C, N, O, S, Si, Fe and Mg, whose abundances have been assumed to be solar. The temporal evolution of the ionization of H is followed by integrating, along with the fluid equations, the evolution equation 6 for the number fraction of neutral hydrogen atoms  $f_n$  [Rossi et al., 1997]. The charge-exchange mechanism with H is applied for the other elements. Furthermore we assume that the gas never becomes doubly ionized. Density sensitivity of the emission lines is considered for forbidden lines having critical densities below  $10^5 \text{ cm}^{-3}$ .  $\Lambda_c$  in Eq. 4 then represents the energy loss term (energy per unit volume per unit time) which includes energy lost in lines and in the ionization and recombination processes. This cooling treatment is valid for shock velocities below about  $80 \text{ km s}^{-1}$  and temperatures up to  $T \approx 4 \times 10^4 \text{ K}$ .

[Teşileanu et al., 2008] extended the SNEq treatment, where the electrons from hydrogen ionization are considered only, to a more general MINEq (Multi-Ion Non-Equilibrium cooling), where the line emission can be computed in conditions of non-equilibrium ionization for 29 ion species, whose number fraction was obtained by solving the corresponding temporal evolution equations, analogous to Eq. 6. Tests performed by the authors have shown that a major advantage obtained by using MINEq, compared to SNEq, was that the line emission could be computed in conditions of non-equilibrium ionization for all species, more likely to be encountered in situations of rapid changes, as it is the case of strong shock waves. However, jet simulations with typical post-shock temperatures in the range  $1.5 - 4 \times 10^4$  K yielded morphologies similar between the SNEq and MINEq runs, since at these temperatures the two cooling loss functions are comparable.

The degree of ionization is governed by an additional evolutionary equation,

$$\frac{\partial f_n}{\partial t} + (\mathbf{v} \cdot \nabla) f_n = -n_e \left[ \left( c_i + \frac{\zeta_x}{n_e} \right) f_n + c_r (1 - f_n) \right], \quad (6)$$

where  $f_n = n_{\text{HI}}/n_{\text{H}}$  is the neutral hydrogen fraction,  $n_e$  is the electron density while  $c_i$  and  $c_r$  are respectively, the ionization and recombination rate coefficients [Rossi et al., 1997] given by,

$$c_i = \frac{1.08 \times 10^{-8} \sqrt{T}}{(13.6)^2} \cdot \exp\left(-\frac{157890}{T}\right) \text{ cm}^3 \text{ s}^{-1}, \quad (7)$$

$$c_r = 2.6 \times 10^{-11} \sqrt{T} \text{ cm}^3 \text{ s}^{-1},$$

where  $T$  is temperature (in Kelvin). The additional term  $\zeta_x$  account for photoionization and it is described below.

The  $\mathcal{H}_x$  term takes into account the energy input by stellar X-rays photons which, in the Kev energy range, can potentially result in the production of fast primary photoelectrons after interacting with gas atoms (or molecules). Primary photoelectrons, in turn, generates collisionally a deal of secondary electrons [Glassgold et al., 1997]. We follow the treatment by [Shang et al., 2002] that ignores the contribution of the primary electrons and considers the dominant secondary electrons only. The X-rays optical depth is

$$\tau_x = \sigma_{pe}(kT_x) N, \quad N = \int_0^r n_H(r) dr, \quad (8)$$

where  $\sigma_{pe}(E) = \sigma_{pe}(kT_x)(\text{keV}/E)^p$ . For solar abundances,  $p = 2.485$ ,  $kT_x = 1\text{keV}$  and  $\sigma_{pe}(1\text{keV}) = 2.27 \times 10^{-22} \text{ cm}^2$ . We write the energy input  $\mathcal{H}_x$  by X-rays (energy per unit volume per unit time) and the ionization rate due to the secondary electrons  $\zeta_x$  as

$$\zeta_x = \frac{1}{4\pi r^2} \int_{E_0}^{\infty} \frac{L_x(E)}{\epsilon_{\text{ion}}} \sigma_{pe}(E) e^{-\tau_x} dE. \quad (9)$$

In the expression above  $L_x(E)$  is the X-ray luminosity per unit energy interval [Shang et al., 2002],  $E_0 (= 0.1\text{keV})$  is the low-energy cutoff,  $y_{\text{heat}}$  is the absorbed fraction of the X-ray flux, and  $\epsilon_{\text{ion}}$  the energy to make an ion pair. Since  $y_{\text{heat}}$  and  $\epsilon_{\text{ion}}$  can be considered nearly independent of energy, we have

$$\mathcal{H}_x = n_H(r)y_{\text{heat}}\epsilon_{\text{ion}}\zeta_x \quad (10)$$

where [Shull and van Steenberg, 1985]

$$\frac{1}{\epsilon_{\text{ion}}} = \frac{y_H}{I_H} + \frac{y_{\text{He}}}{I_{\text{He}}}, \quad (11)$$

with

$$\begin{aligned} y_H &= 0.3908 (1 - x_e^{0.4092})^{1.7592}, \\ y_{\text{He}} &= 0.0554 (1 - x_e^{0.4614})^{1.666}. \end{aligned} \quad (12)$$

In the above relationships  $I_H$  and  $I_{\text{He}}$  are the ionization potentials of  $H$  and  $He$ ,  $x_e$  is the hydrogen ionization fraction and

$$y_{\text{heat}} = 0.9971 \left[ 1 - (1 - x_e^{0.2663})^{1.3163} \right] \quad (13)$$

specifies the heating fraction. Note that for a thermal spectrum, the ionization rate Eq. (9) takes the form

$$\zeta_x = \frac{L_x \sigma_{pe}(kT_x)}{4\pi r^2 \epsilon_{\text{ion}}} \int_{\zeta_0}^{\infty} \xi^{-p} \exp[-(\xi + \tau_x \xi^{-p})] d\xi, \quad (14)$$

where  $L_x$  is now the total integrated luminosity in  $[E_0, \infty]$ .

We will also follow the temporal evolution of a passive 'tracer'  $\mathcal{T}$  which is advected by the fluid motion and obeys the simple transport equation

$$\frac{\partial(\rho\mathcal{T}_{AJ})}{\partial t} + \nabla \cdot (\rho\mathcal{T}_{AJ}\mathbf{v}) = 0. \quad (15)$$

The addition of a passive scalar will be useful to discriminate between the jet material accelerated due to magneto centrifugal mechanism and the jet in the axis, see §3.1.

## 2.2 Numerical Approach

The MHD Eqns. (1)-(4) together with (6) are solved in 2D axisymmetric cylindrical coordinates  $(R, z)$  using the PLUTO code with adaptive mesh refinement [Mignone et al., 2012]. The computational domain is defined by the rectangular box  $R \in [0, R_{\text{end}}]$ ,  $z \in [0, z_{\text{end}}]$ , where  $R_{\text{end}} = 125 \text{ AU}$  while  $z_{\text{end}} = 2000 \text{ AU}$ . We employ 5 levels of refinement starting from a base grid of  $128 \times 2048$  zones yielding an equivalent resolution of  $4096 \times 65536$ .

A globally 2<sup>nd</sup> order Runge-Kutta scheme with linear spatial reconstruction is used to evolve the equations in time. Slope limiter in curvilinear coordinates are obtained using the procedure of [Mignone, 2014] to prevent loss of

accuracy near to the coordinate origin. The van Leer limiter is applied to primitive flow quantities. The equations are solved in conservative form by evaluating inter-zone numerical fluxes resulting from the (approximate) solution of Riemann problems at zone interfaces. For the present work, we employ the Harten Lax van Leer (HLL) Riemann solver. The divergence-free condition of magnetic field is enforced using hyperbolic divergence cleaning as described in [Mignone and Tzeferacos, 2010, Mignone et al., 2012].

We employ a combination of static mesh refinement, close to the central object, as well as dynamic mesh refinement as the outflow propagates outwards. More specifically, the region within 20 AU is always covered with 4 refinement levels with one additional level (level 5) in the innermost region ( $\lesssim 8$  AU). Outside of this region but close to the disk boundary ( $R > 20$  AU,  $z < 5$  AU), the refinement is also static but only 3 levels are used. Everywhere else the grid is refined dynamically using the second-derivative of pressure (although no more than 3 levels are permitted).

We point out that high resolution is essential close to the central object in order to properly resolve the photionization process which takes place on a much smaller scale when compared to the overall size of the domain.

### 2.2.1 Evaluation of the Heating Term

Evaluation of the heating term, Eq. (10), requires some additional considerations as the integral in Eq. (14) depends the optical depth  $\tau_x$  (Eq. 8) which, in principle, should be computed by ray-tracing integration from the central star to the current zone position. However, in practice, the integral in Eq. (14) becomes negligible at a distance of  $\gtrsim 20AU$ , so that only the statically refined patches around the star yield a significant contribution.

Ray tracing is then performed as follows: each zone  $(i, j)$  is connected to the origin by a ray divided into  $m$  equally spaced segments. The optical depth is then evaluated using a trapezoidal rule,

$$N_{ij} \approx \sum_{k=0}^{m-1} \left( \frac{\rho_k + \rho_{k+1}}{2} \right) \Delta r_{ij}, \quad (16)$$

where  $\rho_k$  is obtained using bi-linear interpolation,  $\Delta r_{ij} = r_{ij}/m$  while  $r_{ij} = (r_i^2 + z_j^2)^{\frac{1}{2}}$  is the spherical radius. In order to have approximately equal sampling on all rays, we set  $m = \text{int}(r_{ij}/\Delta r_0) + 1$ , where  $\Delta r_0$  is the diagonal of the first computational cell. Eq. (16) can be readily evaluated on computational patches that includes the system origin. Conversely, if a patch does not fulfill this condition, we still use Eq. (16) to compute the portion of the integral that lie on this grid and then add the contribution coming from the (lower or left) adjacent patch. Since computations are performed in parallel, the full integral will be obtained by joining contributions sequentially over few time steps, since integration has to propagate across grid patches. We have verified (using a single static grid computation) that this does not pose a problem as the solution reach a stationary configuration in a few dynamical time scales.

Finally, in order to speedup the computation of the integral in Eq. (14), we preliminary obtain a table for different values of  $\tau_x$  and then use look table method as in[Vaidya et al., 2015] to obtain the value of an arbitrary value of  $\tau_X$ .

### 3 Setup

We now describe the initial and boundary conditions adopted for our numerical simulations. In what follows we denote with  $R$  the cylindrical radius and with  $r \equiv \sqrt{R^2 + z^2}$  the spherical radius.

#### 3.1 Initial conditions

In order to set the initial conditions in the computational domain, we first define a gravitational potential by placing a central star with mass  $M$  at the coordinate origin

$$\Phi_G = \begin{cases} -\frac{GM}{r_0} \frac{1}{\xi}, & \text{if } \xi > 1, \\ -\frac{GM}{r_0} \left( \frac{7}{4} - \frac{7}{8}\xi^2 + \frac{1}{8}\xi^6 \right) & \text{if } \xi \leq 1. \end{cases} \quad (17)$$

Here  $\xi = r/r_0$  is the spherical radius normalized to the reference length  $r_0$  which we assume to be the inner radius of the Keplerian disk. The smoothing at  $\xi \leq 1$  is set to avoid the singularity of the gravitational potential of a point-like mass. The chosen smoothing sets the gravitational acceleration to zero at the origin, while it preserves the continuity of the gravitational acceleration and its first derivative at  $\xi = 1$ .

The density profile is given by

$$\left( \frac{\rho_c}{\rho_0} \right)^{\gamma-1} = \begin{cases} \frac{1}{\xi}, & \text{if } \xi > 1 \\ \left( \frac{7}{4} - \frac{7}{8}\xi^2 + \frac{1}{8}\xi^6 \right) & \text{if } \xi \leq 1, \end{cases} \quad (18)$$

where  $\rho_0$  is our unit density while  $\gamma = \frac{5}{3}$  is the specific heat ratio. The thermal pressure profile is initially set to  $P_c = P_0 (\rho_c/\rho_0)^\gamma$ , so that the initial corona is isentropic. A value  $P_0 = (\gamma - 1)/\gamma GM\rho_0/r_0$  would correspond to an hydrostatic corona. Such a condition would set the initial temperature around the origin close to the virial value, that for a typical normalization would correspond to  $10^5 - 10^6$  K. Such a high temperature would strongly compromise the computation of the ionization fraction; we therefore decided to impose a much lower temperature using  $P_0 = 0.0024 GM\rho_0/r_0$ . Obviously the corona is not in hydrostatic equilibrium and will tend to collapse towards the origin. This does not represent a problem since this initial corona will be swept-up by the formation of the outflow accelerated from the bottom boundary. While



a magneto-centrifugal mechanism will be responsible for the disk-wind acceleration, this process can not be effective around the symmetry axis. Since we wanted to avoid using a thermal pressure gradient to accelerate the axial part of the jet (it would have introduced high and unrealistic temperatures), we added an artificial accelerating force for the axial jet proportional to gravity. We introduced a passive scalar  $\mathcal{T}_{AJ}$  to follow the matter injected from the bottom boundary in the  $R < r_0$  region, where  $\mathcal{T}_{AJ}$  is injected with a unity value and zero elsewhere. We then define the gravity as  $\mathbf{g} = (1.2\mathcal{T}_{AJ} - 1)\nabla\Phi_G$ , providing an extra push for the axial jet only. In the corona, all the components of the speed are set initially to zero.

The atmosphere (and the disk) is threaded by a large-scale force-free magnetic field which is purely poloidal [Ouyed and Pudritz, 1997] The field is prescribed in terms of the  $\phi$  component of the vector potential,  $\mathbf{B} = \nabla \times (A_\phi \hat{\mathbf{e}}_\phi)$  where

$$A_\phi = B_{z0} \sqrt{r_0^2 + z_d^2} \frac{\sqrt{R^2 + (z + z_d)^2} - (z + z_d)}{R}, \quad (19)$$

so that  $B_z = 1/R \partial_R (R A_\phi)$ ,  $B_R = -\partial_z A_\phi$ . In the expressions above  $z_d$  is considered as a disk thickness (set to  $r_0$ ), and  $B_{z0}$  is the value of the  $z$  component of the magnetic field at  $(R = r_0, z = 0)$ . In order to avoid abrupt changes in the ionization rate, the neutral fractions of hydrogen is set at equilibrium values. The temperature of the corona is  $\sim 10^3$  K at its base, the mean molecular weight is taken to be  $\mu = 0.6$ . Finally, to ensure that the density profiles do not fall below observational limits, we add floor value to the latter  $\rho = 10^{-6} \rho_0$ .

## 3.2 Boundary conditions

The choice of physical boundary conditions is of utmost importance as they will determine the final steady state solution. With the present setup, we have to deal with four boundary regions.

### 3.2.1 Bottom Boundary

The accretion disk is modelled through the boundary condition at  $z \leq 0$ . The disk density is set to be proportional to the initial coronal density so that  $\rho_{\text{disk}}(R) = \chi \rho_c(R, z = 0)$ , where  $\chi = 100$ .

The radial and toroidal magnetic field components  $B_R$  and  $B_\phi$  are set to be continuous across the boundary by linearly extrapolating from the interior zones, while the  $B_z$  component is kept to its initial value in order to conserve the magnetic flux through the disk surface. We want the magnetic field to be frozen in the disk Keplerian rotation, meaning that in a frame of reference locally co-rotating with the disk the electric field  $\mathbf{E} = -\mathbf{v} \times \mathbf{B}$  must be zero. For the toroidal component of the electric field this means that the poloidal speed must be parallel to the poloidal magnetic field. We use the fact that the mass to magnetic flux ratio  $\eta = \rho v_p / B_p$  is invariant along poloidal field lines in a stationary state to extrapolate the poloidal speed from the computational

domain into the boundary. The condition on the poloidal component of the electric field provides the boundary condition for the toroidal speed:

$$v_\phi = v_K + \frac{v_p}{B_p} B_\phi, \quad (20)$$

where the Keplerian velocity profile  $v_K$  is recovered by balancing centrifugal and gravitational terms:

$$v_K = \begin{cases} \sqrt{\frac{GM}{R}}, & \text{if } R > r_0 \\ \sqrt{\frac{GM}{4r_0}} \sqrt{7 \left(\frac{R}{r_0}\right)^2 - 3 \left(\frac{R}{r_0}\right)^6} & \text{if } R \leq r_0. \end{cases} \quad (21)$$

The second term in Eq. (20) accounts for the rotationally induced azimuthal component of the magnetic field. When the simulation starts, in fact, the rotating disk winds up the poloidal field and induces a toroidal field component. Anyway, we don't want the toroidal speed to deviate too much from the Keplerian velocity thus we enforce the value of  $v_p$  so that the toroidal speed is at least half the Keplerian value. The value of  $v_p$  is also limited to be less than half the local sound speed.

The pressure of the disk is set assuming a thermal height scale of the disk in the  $R > r_0$  region, defined through the disk aspect ratio  $\epsilon = c_s/v_K$ , where  $c_s^2 = p/\rho$  is the disk isothermal sound speed. The disk pressure is therefore provided by the expression  $P_{\text{disk}} = \epsilon^2 \chi (\rho_{\text{disk}}/\chi\rho_0)^\gamma GM\rho_0/r_0$ . Notice that also the disk is isentropic and its pressure is proportional to the initial coronal pressure at  $z = 0$ . We set the ionization to be zero (all neutral).

### 3.2.2 Top Boundary Conditions

On the outer right boundary that is  $R = R_{\text{end}}$  outflow condition that is zero gradient are imposed on poloidal velocity components, neutral fraction of hydrogen, tracer and  $B_r$ . For density  $\rho$  thermal pressure  $P$ ,  $v_\phi$ ,  $B_r$  and  $B_\phi$  the continuity on the first derivative is required. The conditions on  $B_z$  is determined by imposing the solenoidality on the field  $\nabla \cdot \mathbf{B} = 0$ .

### 3.2.3 Axial Boundary

Along the jet axis ( $R = 0$ ), axisymmetric boundary conditions are applied. This requires the normal and the toroidal components of vector fields to be antisymmetric, while remaining quantities are symmetric.

### 3.2.4 Outer radial boundary

At the top boundary ( $z = z_{\text{end}}$ ), we impose continuity, up to the first derivative, for  $\rho$ ,  $P$ ,  $v_\phi$ ,  $B_z$  and  $B_\phi$ . Neutral fraction of hydrogen, tracer, radial and vertical velocities are simply copied from the interior zones (outflow condition). The

normal component of the magnetic field,  $B_r$ , follows again from the divergence-free condition.

### 3.2.5 Units

Fluid variables are normalized to their physical values at the inner disk radius  $r_0 = 0.1\text{AU}$  which also sets our unit length. At that point, the Keplerian velocity is

$$V_{k0} = 94 \left( \frac{M}{M_\odot} \right)^{-1/2} \left( \frac{r_0}{0.1 \text{ AU}} \right)^{1/2} \text{ km/s}^{-1}. \quad (22)$$

The time unit follows from  $t_0 = r_0/V_{k0}$ ,

$$t_0 = 1.7 \left( \frac{M}{M_\odot} \right)^{-1/2} \left( \frac{r_0}{\text{AU}} \right)^{3/2} \text{ days}, \quad (23)$$

Densities are given in units of  $\rho_0 = 10^{-18} \text{ gr/cm}^3$

## 4 Results: Adiabatic Case

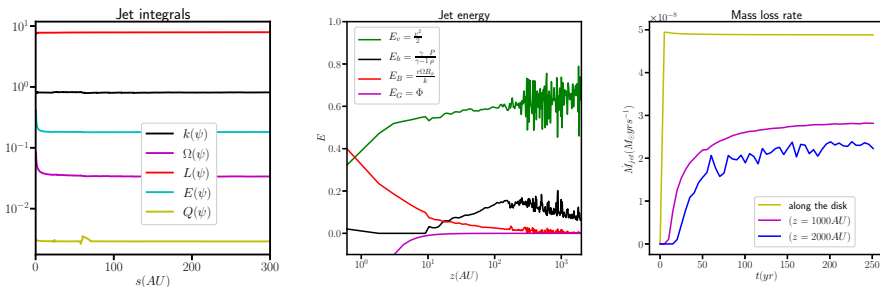


Figure 1: Left panel: Jet integrals along the magnetic field line rooted in the innermost disk. The jet specific angular momentum  $\Omega$ , the mass load  $k$ , the field angular velocity  $L$ , the jet specific energy  $E$ , and the specific entropy  $Q$ . Central panel: Jet specific energy contributions along the vertical direction  $z$ . Different energy components are indicated by colors: kinetic (green), magnetic (red), gravitational (magenta), and thermal (black) energy. Right panel: Mass loss rate as a function of time at different heights (yellow) along the disk, (magenta) at 1000AU and (blue) at 2000AU. The figure show decrease in the ejection as we go further from the disk surface.

In this section we check our numerical results against theoretical predictions by using the adiabatic MHD simulation (no cooling or heating).

### 4.1 Steady state Jet MHD Integrals

In axisymmetric, stationary, ideal MHD there are five quantities that are expected to be conserved along a field line, i.e., a surface of constant magnetic

flux  $\Psi$ , namely the mass to magnetic flux ratio,

$$k(\Psi) = \frac{\rho v_p}{B_p}, \quad (24)$$

the angular velocity of the field lines:

$$\Omega(\Psi) = \frac{1}{r} \left( v_\phi - \frac{k B_\phi}{\rho} \right) \quad (25)$$

the specific angular momentum

$$L(\Psi) = L_v + L_B = r v_\phi - r \frac{B_\phi}{k}, \quad (26)$$

with kinematic and magnetic contribution, and the specific energy

$$E(\Psi) = \frac{v^2}{2} + \frac{\gamma}{\gamma - 1} \frac{P}{\rho} + \Phi - \frac{r \Omega B_\phi}{k}, \quad (27)$$

and the specific entropy,

$$Q(\Psi) = \frac{P}{\rho^\gamma} \quad (28)$$

The left panel in Fig. 1 displays the values of these integrals as a function of position  $s$  along the field line at some advanced stage, when a stationary configuration has been reached. We use a sample field line rooted in the innermost part of the ejection region at a radius  $1.5r_0$  and plot the quantities at  $t = 250$  yrs. The integrals are approximately constant, as expected, showing small deviation with errors that remain below 6%.

## 4.2 Jet energy

In the central panel of Fig. 1 we plot the different contributions to the specific energy of Eq. (27) along the jet vertical direction. The thermal energy is negligible everywhere in the jet while gravitational energy is negligible only far from the disk. The plots further indicates how the transition from a magnetically to kinetically dominated flow takes place at a distance  $\lesssim 10$  AU. Far from the disk the transformation of the magnetic energy into kinetic energy becomes less efficient. This decrease of acceleration is related to the increase of collimation.

## 4.3 Mass loss rate

The mass loss rate is a parameter which is, in principle, accessible by observation. Thus the normalisation of density  $\rho_0 = 10^{-18}$  gr/cm<sup>3</sup> is chosen by setting suitable loss rates  $\dot{M}_0 = r_0^2 \rho_0 V_{k0}$ :

$$\dot{M}_0 = 4.3 \times 10^{-8} \left( \frac{\rho_0}{10^{-18} \text{g cm}^{-3}} \right) \left( \frac{M}{M_\odot} \right)^{1/2} \times \left( \frac{r_0}{\text{AU}} \right)^{3/2} M_\odot \text{yrs}^{-1}, \quad (29)$$

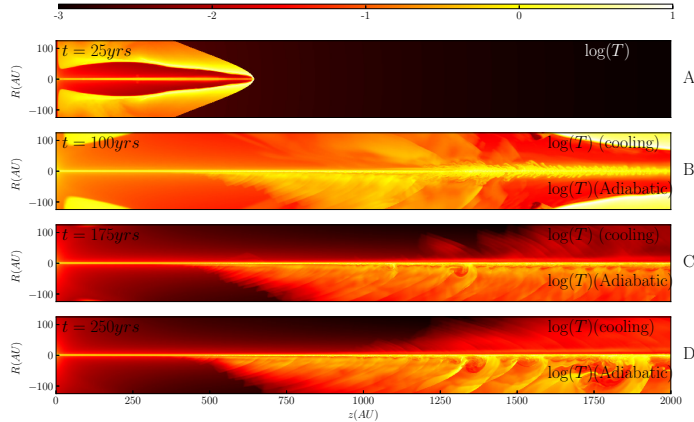


Figure 2: From top to bottom, we show four snapshots of the temporal evolution corresponding to  $t = 25, 100, 175$  and  $250$  yrs. In the first panel (A) shows the logarithmic maps of the temperature (in units of  $10^4$  K) for the adiabatic case. The second three panels (B, C, D) compares the temperature maps when cooling is included (upper half) and the adiabatic case (lower half). The jet propagates from left to right.

We calculate the mass loss rate at different heights in the jet as function of time. To this aim, we consider the mass flowing through a surface  $S_d = \pi R_{\text{end}}^2$  centered around the symmetry axis:

$$\dot{M}_{\text{jet}} = \int_{S_d} \rho \mathbf{v} \cdot d\mathbf{S} \quad (30)$$

The results obtained are shown in the rightmost panel of Fig 1 indicating that the mass loss rate is proportional to  $10^{-8} M_{\odot} \text{ yrs}^{-1}$  and decreases as we move far away from the accretion disk due to losses sideways. The asymptotic values in time at different heights are consistent with observations.

## 5 Results: non-adiabatic Cases

In the non-adiabatic case, cooling and heating are both included in the energy equation Eq. (4) and the degree of ionization is computed by solving Eq. (6). Still, in order to avoid excessive cooling at the jet bow shock, with the consequent strong decrease of the numerical evolution time step, we suppress cooling for  $t \lesssim 40$  yrs of evolution and then gradually turn it on.

### 5.1 Dynamics

The temporal evolution is described by the four panels in Fig. 2, showing temperature maps at four different stages of the evolution. For comparison, the lower panels (B, C, D) show the temperature distributions in the adiabatic

and non-adiabatic cases. During the propagation the jet bow shock is heated to large temperatures ( $T \sim 7 \times 10^4$  K) and unstable flow patterns develop close to the axis.

These perturbations are induced by the combined action of Kelvin-Helmholtz and pressure driven  $m = 0$  modes and tend to grow sideways steepening into oblique shock waves around  $t \approx 100$  yrs. While in the adiabatic case these features persist until later times, they become progressively weaker in the presence of radiative losses (see the third and fourth panels in the figure).

A steady state is finally reached around  $t \approx 250$  yrs. The effect of cooling is also that of reducing the internal energy of the flow by approximately one order of magnitude when compared to the adiabatic run. Owing to the drop in thermal pressure, the jet is more easily collimated towards the axis by the hoop stresses.

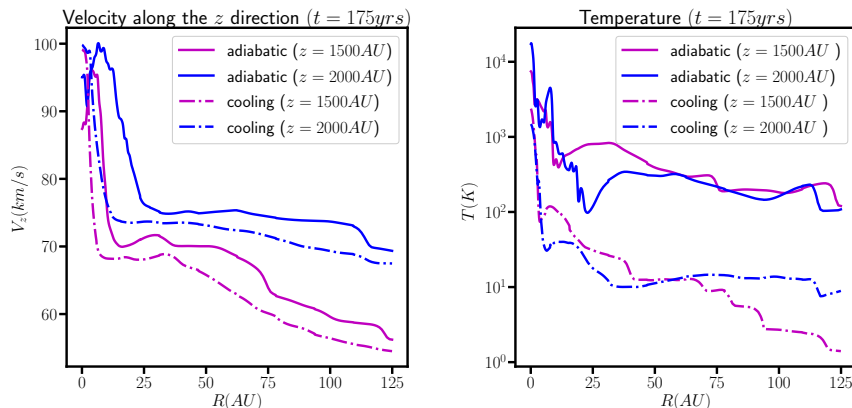


Figure 3: Top panel: velocity along the  $z$  direction in km/s profile - adiabatic and cooling cases, - at different heights. Bottom panel: temperature profile (in K) - adiabatic and cooling cases, - at different heights, corresponding to  $t = 175$  yrs.

The effect of energy losses on the jet dynamics is shown in Fig. 3 where we compare radial profiles of temperature and vertical velocity at different heights of the domain for both the adiabatic and non-adiabatic simulations. Optically thin radiative losses significantly reduce the jet temperature, namely, by one order of magnitude for  $R \lesssim 25$  AU and even more outside of this region. The loss of internal energy reduces the efficiency of the jet thrust and the bulk kinetic energy diminishes. As a consequence, the beam velocity is also reduced (lower panel). The velocity indicates that there is a narrow central spine at high velocity surrounded by an extended low velocity wind. The observations often show the same structure see [Giannini et al., 2019].

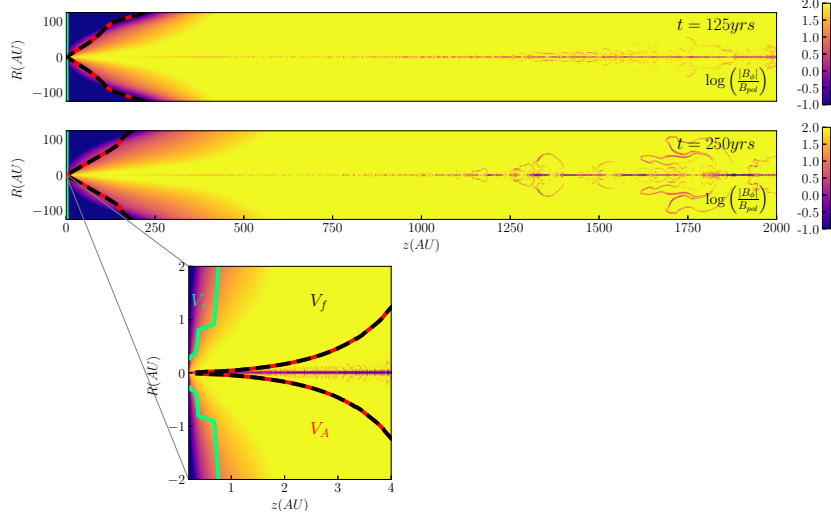


Figure 4: Top panel: From top to bottom, we show two snapshots of the logarithmic ratio of the absolute value of the toroidal magnetic field over the poloidal, the temporal evolution corresponding to  $t = 125$  and  $250$  yrs. The solid lines in (red, black and green) indicate the critical surfaces i.e. Alfvénic, fast magnetosonic and slow magnetosonic respectively. Bottom panel: Zoomed image of the jet base, with logarithmic coordinate along  $z$  indicating the critical surfaces; the solid lines in (red, black and green) corresponds to Alfvénic, fast magnetosonic and slow magnetosonic respectively. The jet propagates from left to right.

### 5.1.1 Magnetic field configuration

The magnetic field configuration, showing the logarithmic ratio of toroidal to poloidal magnetic field components as well as the critical surfaces, is shown in Fig. 4. Critical surfaces are defined as the isosurfaces where the poloidal velocity component becomes equal to one of the three MHD wave speeds:

$$\begin{aligned}
 V_A^2 &= \frac{B^2}{\rho} \\
 V_{f,s}^2 &= \frac{(C_s^2 + V_A^2) \pm \sqrt{(C_s^2 + V_A^2)^2 - 4C_s^2 V_{Ap}^2}}{2},
 \end{aligned} \tag{31}$$

where  $V_{Ap}$  is the (poloidal) Alfvénic speed and  $C_s = \sqrt{\gamma p / \rho}$  is the adiabatic speed of sound. The three isosurfaces are plotted as solid lines (red, black and green) corresponding to Alfvénic, fast magnetosonic and slow magnetosonic, respectively. The flow crosses the Alfvénic surface when the bow shock has left the domain and the system has entered a stationary configuration.

The colormap clearly shows that there are two regions where the poloidal component exceeds the toroidal one, namely, near the disk’s surface and below the Alfvén surface (depicted in cyan solid line). Close to the disk

component is dominant to impose the co-rotation of the outflow. Conversely, above the Alfvén surface co-rotation stops and the azimuthal component dominates so that the main driving force is the gradient of magnetic pressure of  $B_\phi$ . For a complete description of the mechanism see [Blandford and Payne, 1982].

## 5.2 Ionization

Next we investigate the effect of cooling and heating on the amount of ionization produced during the evolution. To this purpose, we compare two different simulation cases, the former including the optically thin losses alone and the latter also introducing the heating term due to photionization.

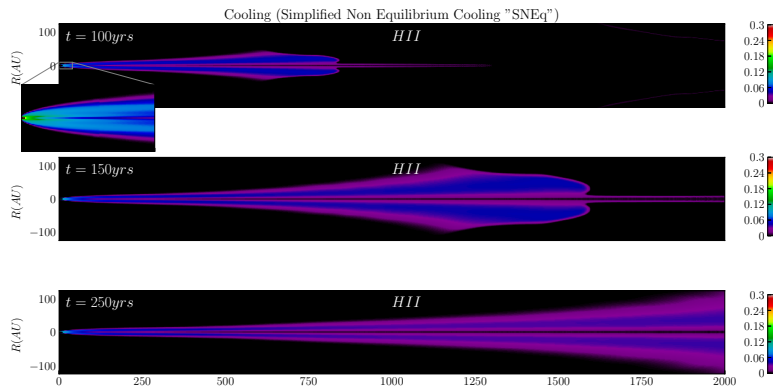


Figure 5: SNEq (Simplified Non Equilibrium Cooling): Ionization fraction of the jet material when only cooling is included (no heating). Snapshots are shown at  $t = 100, 150$  and  $t = 250$  yrs.

In the first case, only  $\sim 10\%$  of the hydrogen becomes ionized close to the central object and recombination takes place as the flow propagates outward, eventually lowering this value to less than 4% at large distances. This situation is best illustrated in Fig. 5 where we display 2D maps of the ionization fraction at  $t = 100, 150$  and  $250$  yrs, when steady state is eventually reached. The ionization area is initially small ( $\sim 2$  AU) and it expands conically reaching  $\sim 120$  AU at the end of the domain. These results are consistent with the idea that the ionisation is persisting, while travelling away from the source see [Bacciotti and Eisloffel, 1999].

In the second case (Fig. 6, lower panels) we compare different evolutionary snapshots for two different simulations, corresponding to a high luminosity case ( $L_x = 10^{32}$  erg/s, upper half of each panel) and a low luminosity case ( $L_x = 10^{28}$  erg/s lower half of each panel). While the latter does not produce any noticeable difference in the amount of ionization when compared to the purely radiative case (see Fig. 5), the former results in an appreciably larger ionization rate. Close to the central object we now observe almost  $\sim 50\%$



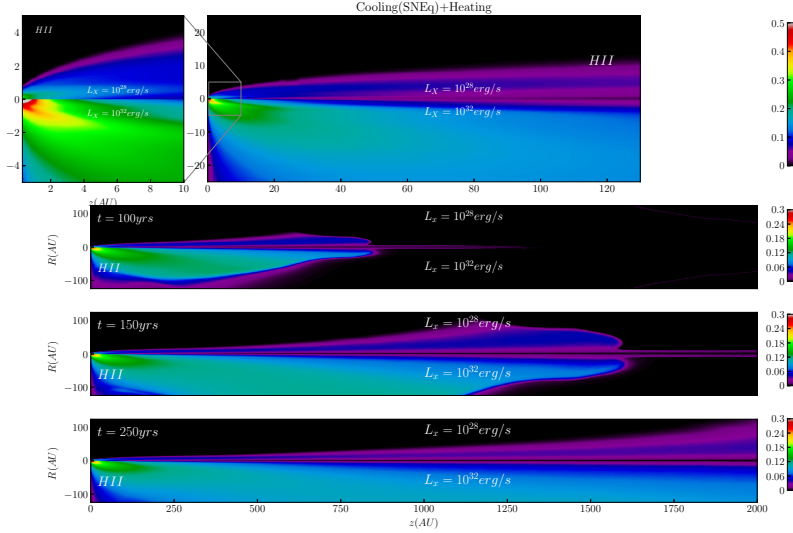


Figure 6: (SNEq+Heating) Bottom panel: Maps of the total ionization fraction of the jet material for different luminosity  $L_X = 10^{28} \text{ erg/s}$ ,  $L_X = 10^{32} \text{ erg/s}$  at different times  $t = 100, 150$  and  $t = 250$  yrs. Top panel: The corresponding zoomed image of total hydrogen ionization fraction at time  $t = 100$  yrs.

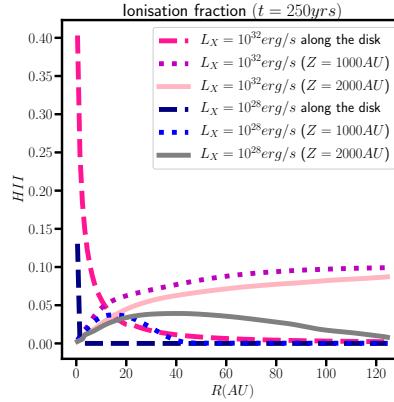


Figure 7: Ionisation fraction profiles for different luminosity  $L_X = 10^{28} \text{ erg/s}$ ,  $L_X = 10^{32} \text{ erg/s}$  at different heights, corresponding to  $t = 250$  yrs.

ionization degree, lowering to  $\sim 10\%$  at large distances (see the zoomed image below). The ionization area is now also much larger extending to  $R = 120 \text{ AU}$  with 10% of ionisation fraction, reaching the outer radial boundary at  $z = 2000 \text{ AU}$  see (Fig. 7). Ions can survive large distance propagation owing to the rather long recombination scale.

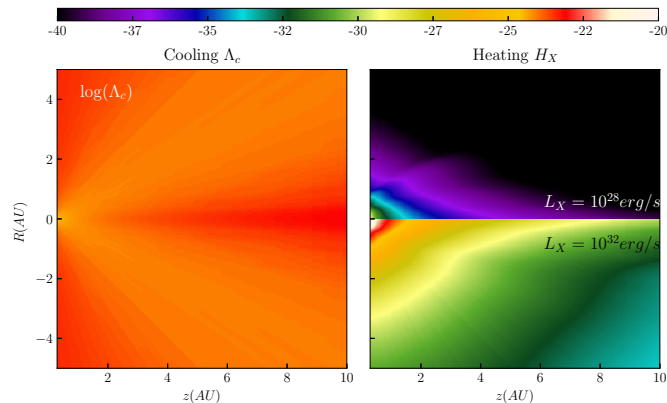


Figure 8: Left panel: Zoomed logarithmic 2D map of the cooling  $\Lambda_c$  in  $\text{erg cm}^{-3} \text{s}^{-1}$ . Right panel: Zoomed image of the logarithmic 2D heating map  $\mathcal{H}_X$  in  $\text{erg cm}^{-3} \text{s}^{-1}$ , for luminosity  $L_X = 10^{32} \text{erg/s}$  and  $L_X = 10^{28} \text{erg/s}$ , at  $t = 150 \text{ yrs}$ .

A close-up of the central region is shown in the top panel of Fig. 6 at  $t = 150 \text{ yrs}$  for both the low and high luminosity cases. Here we show a composite image of the ionization fractions for  $z < 130 \text{ AU}$  (bottom larger panel) and a smaller view of the central region ( $z < 10 \text{ AU}$ ) (upper, left panel). From the figure it is evident that the jet is ionized by  $\sim 50\%$  close to the star ( $R \lesssim 2 \text{ AU}$ ) owing to the strong photo-ionizing X-rays flux of the high luminosity case. This fraction decreases to the nominal value of  $10 - 20\%$  and it is essentially transported as the jet propagates outwards. In Fig. 8 we include both cooling and heating maps, the latter case being split into the low- and high-luminosity case. Heating is stronger close to the origin reaching peak values in the range  $10^{-20} - 10^{-23} \text{ erg cm}^{-3} \text{ s}^{-1}$  and thus appreciably larger than cooling. Heating is then quickly suppressed with distance as the luminosity decreases as  $1/R^2$  becoming negligible already beyond a distance of  $\approx 3 \text{ AU}$  where cooling overwhelms ( $\Lambda_c$  is about  $10^{-24} \text{ erg cm}^{-3} \text{ s}^{-1}$ ). This results is in agreement with the work of [Teşileanu et al., 2008].

These results confirm and validate the assumption that photoionizing X-rays from the central star can be held responsible for the inferred ionization rates at very large distances [Teşileanu et al., 2012]. They have shown that shocks propagating along the jet in a medium that has been pre-ionized at a ratio of about 20% give off-line emission from the post-shock region that well matches the observed surface brightness, especially at distances above few hundreds AU. Without pre-ionization, the post-shock brightness falls short by about an order of magnitude with respect to observations of the jet in RW Aurigae see [Teşileanu et al., 2012].

## 6 Summary and conclusions

By means of high-resolution MHD numerical computations we have investigated the effect of stellar-driven X-ray photoionization on the jet launching and its subsequent large scale propagation up to 2000 AU. Owing to the large disparities in temporal and spatial scales, numerical simulations have been conducted using adaptive mesh refinement with the PLUTO code using 2D cylindrical axisymmetric coordinates. The outflow is magnetically driven by the accretion disk which is treated as boundary condition. Both optically thin cooling and X-ray heating have been included in our model. Owing to the small X-ray photon mean-free-path and geometrical dilution, heating is effective only at a distance of few AU from the central star. For typical X-ray luminosities in classical T-Tauri stars ( $10^{28} \text{ erg/s} \lesssim L_x \lesssim 10^{32} \text{ erg/s}$ ), we observe that photoionization is capable of ionizing the jet material up to  $\sim 50\%$  (for the highest luminosity case) close to the central object. Because of the slow recombination rates, ionized material can survive large scale propagation reaching steady state asymptotic values of  $\sim 10 - 20\%$  far from the launching region, in agreement with the assumption made by [Teşileanu et al., 2012].

We have also confirmed that the ejection rate, temperature, and velocity are within the typical value range of observed astronomical sources. In a future work, we plan to model specific YSO jets with the inclusion of shocks along the beam generated by the application of variability of the ejection process at the base of the outflow. Synthetic maps will be produced with a post-processing code that calculates the emission starting from the gas physical parameters determined by the output of the dynamical simulation. Such maps will be compared with observed maps at high angular resolution.

**Acknowledgements** We thank an anonymous referee for his/her criticisms, suggestions and comments that have greatly helped to improve the paper. We are grateful to Dr. Bhargav Vaidya, Asst. Professor, Centre of Astronomy (IIT Indore), Indian Institute of Technology Indore for insightful discussion. We acknowledge the CINECA award under the ISCRA initiative, for the availability of high performance computing resources and support. Z. Ahmane was supported by the Programme National Exceptionnel (P.N.E) within the Ministry of Higher Education of Algeria and by the predoc scholarship funded by the University of Torino.

## References

- [Bacciotti and Eisloffel, 1999] Bacciotti, F. and Eisloffel, J. (1999). Ionization and density along the beams of herbig-haro jets. *A&A*, 342:717–735.
- [Bacciotti et al., 2002] Bacciotti, F., Ray, T. P., Mundt, R., Eisloffel, J., and Solf, J. (2002). Hubble space telescope/stis spectroscopy of the optical outflow from dg tauri: Indications for rotation in the initial jet channel. *ApJ*, 576(1):222.

- [Bally et al., 2003] Bally, J., Feigelson, E., and Reipurth, B. (2003). X-rays from the vicinity of the protostar I1551 IRS 5: Reflection or fast shocks? *ApJ*, 584(2):843.
- [Bally et al., 2007] Bally, J., Reipurth, B., and Davis, C. J. (2007). Observations of jets and outflows from young stars. *Protostars and Planets V*, pages 215–230.
- [Blandford and Payne, 1982] Blandford, R. and Payne, D. (1982). Hydromagnetic flows from accretion discs and the production of radio jets. *MNRAS*, 199(4):883–903.
- [Cabrit et al., 1990] Cabrit, S., Edwards, S., Strom, S. E., and Strom, K. M. (1990). Forbidden-line emission and infrared excesses in T Tauri stars—evidence for accretion-driven mass loss? *ApJ*, 354:687–700.
- [Cai et al., 2008] Cai, M. J., Shang, H., Lin, H.-H., and Shu, F. H. (2008). X-winds in action. *ApJ*, 672(1):489.
- [Casse and Keppens, 2002] Casse, F. and Keppens, R. (2002). Magnetized accretion-ejection structures: 2.5-dimensional magnetohydrodynamic simulations of continuous ideal jet launching from resistive accretion disks. *ApJ*, 581(2):988.
- [Cox and Raymond, 1985] Cox, D. and Raymond, J. (1985). Preionization-dependent families of radiative shock waves. *ApJ*, 298:651–659.
- [De Colle et al., 2008] De Colle, F., Raga, A. C., and Esquivel, A. (2008). The dynamics of internal working surfaces in magnetohydrodynamic jets. *ApJ*, 689(1):302.
- [Dopita, 1978] Dopita, A. (1978). The Herbig-Haro objects in the Gum nebula. *A&A*, 63:237–241.
- [Dougados et al., 2000] Dougados, C., Cabrit, S., Lavalley, C., and Ménard, F. (2000). T Tauri stars microjets resolved by adaptive optics. *A&A*, 357:L61–L64.
- [Eisloffel and Mundt, 1992] Eisloffel, J. and Mundt, R. (1992). Proper motion measurements in the HH34 jet and its associated bow shocks. *A&A*, 263:292–300.
- [Eisloffel et al., 1994] Eisloffel, J., Mundt, R., and Böhm, K.-H. (1994). Structure and proper motions in Herbig-Haro objects 1 and 2. *ApJ*, 108:1042–1055.
- [Favata et al., 2002] Favata, F., Fridlund, C., Micela, G., Sciortino, S., and Kaas, A. (2002). Discovery of x-ray emission from the protostellar jet I1551 IRS5 (HH 154). *A&A*, 386(1):204–210.
- [Fendt, 2006] Fendt, C. (2006). Collimation of astrophysical jets: The role of the accretion disk magnetic field distribution. *ApJ*, 651(1):272.

- [Fendt, 2009] Fendt, C. (2009). Formation of protostellar jets as two-component outflows from star-disk magnetospheres. *ApJ*, 692(1):346.
- [Gardner et al., 2017] Gardner, C. L., Jones, J. R., and Vargas, P. B. (2017). Numerical simulation of surface brightness of astrophysical jets. *arXiv preprint arXiv:1706.03819*.
- [Giannini et al., 2019] Giannini, T., Nisini, B., Antonucci, S., Biazzo, K., Alcalá, J. M., Bacciotti, F., Fedele, D., Frasca, A., Harutyunyan, A., Munari, U., Rigliaco, E., and Vitali, F. (2019). GIARPS High-Resolution Observations of T Tauri Stars (GHOsT). I. Jet Line Emission. *Astronomy & Astrophysics*, 631:A44.
- [Glassgold et al., 1997] Glassgold, A., Najita, J., and Igea, J. (1997). Erratum:” x-ray ionization of protoplanetary disks” (apj, 480, 344 [1997]). *ApJ*, 485(2):920.
- [Hardee et al., 1997] Hardee, P. E., Stone, J. M., and Xu, J. (1997). Theory and Simulation of Asymmetrically Perturbed Radiatively Cooled Jets. In Wickramasinghe, D. T., Bicknell, G. V., and Ferrario, L., editors, *IAU Colloq. 163: Accretion Phenomena and Related Outflows*, volume 121 of *ASP Conference Series*, page 575.
- [Hartigan et al., 1995] Hartigan, P., Edwards, S., and Ghandour, L. (1995). Disk accretion and mass loss from young stars. *ApJ*, 452:736.
- [Hartigan et al., 1994] Hartigan, P., Morse, J. A., and Raymond, J. (1994). Mass-loss rates, ionization fractions, shock velocities, and magnetic fields of stellar jets. *ApJ*, 436:125–143.
- [Lada, 1985] Lada, C. J. (1985). Cold outflows, energetic winds, and enigmatic jets around young stellar objects. *Annu. Rev. Astron. Astrophys.*, 23(1):267–317.
- [Lavalley et al., 1997] Lavalley, C., Cabrit, S., Dougados, C., Ferruit, P., and Bacon, R. (1997). Sub-arcsecond morphology and kinematics of the dg tauri jet in the [oi] lambda6300 line. *A&A*, 327:671–680.
- [Lavalley-Fouquet et al., 2000] Lavalley-Fouquet, C., Cabrit, S., and Dougados, C. (2000). Dg tau: A shocking jet. *A&A*, 356:L41–L44.
- [Livio, 1999] Livio, M. (1999). Astrophysical jets: a phenomenological examination of acceleration and collimation. *Physics Reports*, 311(3-5):225–245.
- [Massaglia et al., 2005] Massaglia, S., Mignone, A., and Bodo, G. (2005). Time-dependent mhd shocks and line emission: the case of the dg tau jet. *A&A*, 442(2):549–554.
- [Massaglia et al., 1992] Massaglia, S., Trussoni, E., Bodo, G., Rossi, P., and Ferrari, A. (1992). Radiative unstable modes in the jets of young stellar objects. *A&A*, 260:243–249.

- [Matsakos et al., 2009] Matsakos, T., Massaglia, S., Trussoni, E., Tsinganos, K., Vlahakis, N., Sauty, C., and Mignone, A. (2009). Two-component jet simulations. ii. combining analytical disk and stellar mhd outflow solutions. *A&A*, 502(1):217–229.
- [Matsakos et al., 2008] Matsakos, T., Tsinganos, K., Vlahakis, N., Massaglia, S., Mignone, A., and Trussoni, E. (2008). Two-component jet simulations. i. topological stability of analytical mhd outflow solutions. *A&A*, 477(2):521–533.
- [Matsakos et al., 2012] Matsakos, T., Vlahakis, N., Tsinganos, K., Karampelas, K., Sauty, C., Cayatte, V., Matt, S. P., Massaglia, S., Trussoni, E., and Mignone, A. (2012). Velocity asymmetries in young stellar object jets. Intrinsic and extrinsic mechanisms. *A&A*, 545:A53.
- [Maurri et al., 2014] Maurri, L., Bacciotti, F., Podio, L., Eisloffel, J., Ray, T., Mundt, R., Locatelli, U., and Coffey, D. (2014). Physical properties of the jet from dg tauri on sub-arcsecond scales with hst/stis. *A&A*, 565:A110.
- [Meliani et al., 2006] Meliani, Z., Casse, F., and Sauty, C. (2006). Two-component magnetohydrodynamical outflows around young stellar objects—interplay between stellar magnetospheric winds and disc-driven jets. *A&A*, 460(1):1–14.
- [Melnikov et al., 2009] Melnikov, S. Y., Eisloffel, J., Bacciotti, F., Woitas, J., and Ray, T. P. (2009). Hst/stis observations of the rw aurigae bipolar jet: mapping the physical parameters close to the source. *A&A*, 506(2):763–777.
- [Micono et al., 2000] Micono, M., Bodo, G., Massaglia, S., Rossi, P., Ferrari, A., and Rosner, R. (2000). Kelvin-helmholtz instability in three dimensional radiative jets. *A&A*, 360:795–808.
- [Mignone, 2014] Mignone, A. (2014). High-order conservative reconstruction schemes for finite volume methods in cylindrical and spherical coordinates. *J. Comput. Phys.*, 270:784–814.
- [Mignone et al., 2007] Mignone, A., Bodo, G., Massaglia, S., Matsakos, T., Tesileanu, O., Zanni, C., and Ferrari, A. (2007). Pluto: A numerical code for computational astrophysics. *Astrophys. J. Suppl. Ser.*, 170:228–242.
- [Mignone and Tzeferacos, 2010] Mignone, A. and Tzeferacos, P. (2010). A second-order unsplit godunov scheme for cell-centered mhd: The ctu-glm scheme. *J. Comput. Phys.*, 229(6):2117–2138.
- [Mignone et al., 2012] Mignone, A., Zanni, C., Tzeferacos, P., van Straalen, B., Colella, P., and Bodo, G. (2012). The pluto code for adaptive mesh computations in astrophysical fluid dynamics. *ApJS*, 198(1):7.

- [Moraghan et al., 2006] Moraghan, A., Smith, M. D., and Rosen, A. (2006). Velocity study of axisymmetric protostellar jets with molecular cooling. *MNRAS*, 371(3):1448–1458.
- [Mundt, 1986] Mundt, R. (1986). Jets from young stars: estimates of their physical parameters. *Can.J.Phys.*, 64(4):407–413.
- [Ouyed and Pudritz, 1997] Ouyed, R. and Pudritz, R. E. (1997). Numerical simulations of astrophysical jets from keplerian disks. i. stationary models. *ApJ*, 482(2):712.
- [Raga and Cantó, 1995] Raga, A. and Cantó, J. (1995). The initial stages of an hh jet/cloud core collision. *RevMexAA*, 31:51–61.
- [Ramsey and Clarke, 2011] Ramsey, J. P. and Clarke, D. A. (2011). Simulating protostellar jets simultaneously at launching and observational scales. *ApJ L*, 728(1):L11.
- [Ray et al., 1996] Ray, T. P., Mundt, R., Dyson, J. E., Falle, S. A., and Raga, A. C. (1996). Hubble space telescope observations of jets from young stars. *Astrophys. J. Lett.*, 468(2):L103.
- [Reipurth et al., 1986] Reipurth, B., Bally, J., Graham, J., Lane, A. P., and Zealey, W. (1986). The jet and energy source of hh 34. *A&A*, 164:51–66.
- [Rossi et al., 1997] Rossi, P., Bodo, G., Massaglia, S., and Ferrari, A. (1997). Evolution of kelvin-helmholtz instabilities in radiative jets. ii. shock structure and entrainment properties. *A&A*, 321:672–684.
- [Rubini et al., 2014] Rubini, F., Maurri, L., Inghirami, G., Bacciotti, F., and Del Zanna, L. (2014). Numerical simulations of stellar jets and comparison between synthetic and observed maps: clues to the launch mechanism. *A&A*, 567:A13.
- [Sauty et al., 2002] Sauty, C., Trussoni, E., and Tsinganos, K. (2002). Nonradial and nonpolytropic astrophysical outflows. v. acceleration and collimation of self-similar winds. *A&A*, 389:1068–1085.
- [Sauty and Tsinganos, 1994] Sauty, C. and Tsinganos, K. (1994). Nonradial and nonpolytropic astrophysical outflows III. A criterion for the transition from jets to winds. *A&A*, 287:893–926.
- [Schwartz, 1975] Schwartz, R. (1975). T tauri nebulae and herbig-haro nebulae—evidence for excitation by a strong stellar wind. *ApJ*, 195:631–642.
- [Shang et al., 2002] Shang, H., Glassgold, A. E., Shu, F. H., and Lizano, S. (2002). Heating and ionization of x-winds. *ApJ*, 564(2):853.
- [Shu et al., 1994] Shu, F., Najita, J., Ostriker, E., Wilkin, F., Ruden, S., and Lizano, S. (1994). Magnetocentrifugally driven flows from young stars and disks. 1: A generalized model. *ApJ*, 429:781–796.

- [Shull and van Steenberg, 1985] Shull, J. M. and van Steenberg, M. E. (1985). X-ray secondary heating and ionization in quasar emission-line clouds. *ApJ*, 298:268–274.
- [Skinner et al., 2011] Skinner, S. L., Audard, M., and Güdel, M. (2011). Chandra evidence for extended x-ray structure in ry tau. *ApJ*, 737(1):19.
- [Stone et al., 1997] Stone, J. M., Xu, J., and Hardee, P. E. (1997). The stability of radiatively cooling jets. ii. nonlinear evolution. *ApJ*, 483(1):136.
- [Teşileanu et al., 2009] Teşileanu, O., Massaglia, S., Mignone, A., Bodo, G., and Bacciotti, F. (2009). Time-dependent mhd shocks and line intensity ratios in the hh 30 jet: a focus on cooling function and numerical resolution. *A&A*, 507(2):581–588.
- [Teşileanu et al., 2014] Teşileanu, O., Matsakos, T., Massaglia, S., Trussoni, E., Mignone, A., Vlahakis, N., Tsinganos, K., Stute, M., Cayatte, V., and Sauty, C. (2014). Young stellar object jet models: From theory to synthetic observations. *A&A*, 562.
- [Teşileanu et al., 2008] Teşileanu, O., Mignone, A., and Massaglia, S. (2008). Simulating radiative astrophysical flows with the pluto code: a non-equilibrium, multi-species cooling function. *A&A*, 488(1):429–440.
- [Teşileanu et al., 2012] Teşileanu, O., Mignone, A., Massaglia, S., and Bacciotti, F. (2012). Numerical simulations of radiative magnetized herbig–haro jets: The influence of pre-ionization from x-rays on emission lines. *ApJ*, 746(1):96.
- [Tzeferacos et al., 2009] Tzeferacos, P., Ferrari, A., Mignone, A., Zanni, C., Bodo, G., and Massaglia, S. (2009). On the magnetization of jet-launching discs. *MNRAS*, 400(2):820–834.
- [Uchida and Shibata, 1985] Uchida, Y. and Shibata, K. (1985). Magnetodynamical acceleration of co and optical bipolar flows from the region of star formation. *PASJ*, 37:515–535.
- [Vaidya et al., 2015] Vaidya, B., Mignone, A., Bodo, G., and Massaglia, S. (2015). Astrophysical fluid simulations of thermally ideal gases with non-constant adiabatic index: numerical implementation. *A&A*, 580.
- [Zanni et al., 2007] Zanni, C., Ferrari, A., Rosner, R., Bodo, G., and Massaglia, S. (2007). Mhd simulations of jet acceleration from keplerian accretion disks—the effects of disk resistivity. *A&A*, 469(3):811–828.